

Waves and the equilibrium range at Ocean Weather Station P

J. Thomson,¹ E. A. D'Asaro,¹ M. F. Cronin,² W. E. Rogers,³ R. R. Harcourt,¹ and A. Shcherbina¹

Received 6 February 2013; revised 20 September 2013; accepted 29 September 2013; published 8 November 2013.

[1] Wave and wind measurements at Ocean Weather Station P (OWS-P, 50°N 145°W) are used to evaluate the equilibrium range of surface wave energy spectra. Observations are consistent with a local balance between wind input and breaking dissipation, as described by Philips (1985). The measurements include direct covariance wind stress estimates and wave breaking dissipation rate estimates during a 3 week research cruise to OWS-P. The analysis is extended to a wider range of conditions using observations of wave energy spectra and wind speed during a 2 year mooring deployment at OWS-P. At moderate wind speeds (5–15 m/s), mooring wave spectra are in agreement, within 5% uncertainty, with the forcing implied by standard drag laws and mooring wind measurements. At high wind speeds (>15 m/s), mooring wave spectra are biased low, by 13%, relative to the forcing implied by standard drag laws and mooring wind measurements. Deviations from equilibrium are associated with directionality and variations at the swell frequencies. A spectral wave hindcast accurately reproduces the mooring observations, and is used to examine the wind input.

Citation: Thomson, J., E. A. D'Asaro, M. F. Cronin, W. E. Rogers, R. R. Harcourt, and A. Shcherbina (2013), Waves and the equilibrium range at Ocean Weather Station P, *J. Geophys. Res. Oceans*, 118, 5951–5962, doi:10.1002/2013JC008837.

1. Introduction

[2] Ocean surface waves are the result of wind blowing along a fetch distance for a duration of time. The evolution of ocean surface waves is described by the wave-action equation,

$$\frac{d}{dt} \left(\frac{E}{f} \right) + c_g \cdot \nabla \left(\frac{E}{f} \right) = S_{wind} - S_{brk} + S_{nl} \quad (1)$$

in which a wave energy spectrum $E(f, \theta)$ of frequency f and directional components θ propagates at group velocities $c_g(f)$ and is altered by spectral source/sink terms: input from the wind S_{wind} , dissipation via breaking S_{brk} , and non-linear interactions between wave frequencies S_{nl} . This is also called the radiative transfer equation [Young, 1999].

[3] Phillips [1985] postulated that a portion of the wave energy spectrum would be in equilibrium such that the source/sink terms would balance. By assuming wave growth to be slow and flux divergence to be negligible at small scales, the left-hand side of equation (1) would be

zero at first order. The remaining source/sink terms on the right-hand side then participate at first order in the equilibrium range of the energy spectrum E . Assuming wind input S_{wind} scales with the wind friction velocity squared, u_*^2 , as empirically determined by Plant [1982], Phillips [1985] derived an analytic expression for the energy spectrum as a function of wave number k in the equilibrium range, which can be rewritten in terms of frequency f as

$$\frac{E(f)}{2\pi} = \frac{\beta I(p) g u_* f^{-4}}{16\pi^4}, \quad (2)$$

where β is a constant, $I(p)$ is a directional spreading function, g is gravitational acceleration, and u_* is the wind friction velocity. The cyclic frequency f is used throughout; it is related to the radian frequency ω by $f = \frac{\omega}{2\pi}$. The f^{-4} spectral shape was first suggested as a universal form based on observations by Toba [1973], prior to the dynamic justification proposed by Phillips [1985]. An alternate derivation based on a wave number cascade is given by Kitaigorodski [1983]. The f^{-4} form is commonly used in determining the mean square slope of a wave spectrum, which is given by

$$mss = \int \frac{(2\pi f)^4 E(f)}{g^2} df. \quad (3)$$

[4] The implication of equation (2) is that, given β and $I(p)$, wind friction velocity u_* (and thus wind stress) directly controls wave energy spectra levels at high frequencies. More information is required, however, to compare wave energy spectra to a measured wind speed U_z at a given height z (commonly U_{10}). In a constant stress “law

¹Applied Physics Laboratory, University of Washington, Seattle, Washington, USA.

²Pacific Marine Environmental Laboratory, National Oceanic and Atmospheric Administration, Seattle, Washington, USA.

³Naval Research Laboratory, Stennis Space Center, Mississippi, USA.

Corresponding author: J. Thomson, Applied Physics Laboratory, University of Washington, 1013 NE 40th St., Seattle, WA 98105, USA. (jthomson@apl.uw.edu)

of the wall” boundary layer, the vertical profile of horizontal wind velocity is

$$U_z = \frac{u_*}{\kappa} \ln\left(\frac{z}{z_0}\right), \quad (4)$$

where $\kappa = 0.4$ is the Von Karman constant and z_0 is the roughness length. The roughness length is commonly estimated from the *Charnock* [1955] relation

$$z_0 = \frac{\alpha u_*^2}{g}, \quad (5)$$

where α is assumed to be 0.012. Thus, by combining the *Phillips* [1985] equilibrium formulation and the *Charnock* [1955] relation, a wind speed U_z can be estimated from wave energy spectra.

[5] There are known changes in roughness length z_0 due to waves (i.e., deviations from the *Charnock* [1955] relation). These are second-order corrections and typically associated with the nondimensional wave age $\frac{c_p}{u_*}$ or $\frac{c_p}{U_{10}}$, where c_p is the phase speed of the dominant sea. Although roughness length is an important quantity for the wind profile, it is independent of the wave equilibrium hypothesis (equation (2)). This is because u_* uniquely characterizes the surface stress, via $\tau = \rho_a u_*^2$. The roughness length z_0 and profile $U(z)$ thus are addressed here solely for the purpose of comparison with measured wind speeds. More central to the equilibrium concept is the directionality of the waves relative to the wind.

[6] The *Phillips* [1985] nondimensional directional function $I(p)$ in equation (2) integrates over directions θ relative to the wind direction (i.e., $\theta = 0$ indicates waves aligned with the wind), such that

$$I(p) = \int_{-\pi/2}^{\pi/2} \cos^p \theta d\theta, \quad (6)$$

where p is a directional spreading parameter (increasing for narrower directional distributions). Physically, a narrower directional spectrum is more effective at capturing the wind and thus has a higher $I(p)$. In the equilibrium range, *Phillips* [1985] found the ratio of the downwind wave slope to the total wave slope to be $I(p+2)/I(p)$. In their pioneering study of wave slopes, *Cox and Munk* [1954] found this ratio to range from 0.5 to 0.64. *Juszko et al.* [1995] found similar ratios, solving for p values ranging from 0.0 to 12.5, although typically less than 1, and $I(p)$ values ranging from 1.9 to 3.1.

[7] *Juszko et al.* [1995] successfully showed equilibrium over a limited set of conditions (four storms), and obtained a mean value for the constant $\beta = 0.012$ from a range of $0.006 < \beta < 0.024$. Specifically, *Juszko et al.* [1995] showed agreement between the equilibrium stress $\tau = \rho_a u_*^2$ and the stress calculated with standard drag laws [e.g., *Smith*, 1980; *Large and Pond*, 1981] $\tau = \rho_a C_D U_{10}^2$, where C_D is a drag coefficient. *Donelan et al.* [1985] and *Dobson et al.* [1989] suggested that β depends on the wave age, however *Juszko et al.* [1995] found negligible improvement to u_* estimates when incorporating a variable β . The β values in *Juszko et al.* [1995] are consistent with the *Toba*

[1973] constant $\alpha_T = 4\beta I(p)$ of empirical f^{-4} spectra and the observed values of $\alpha_T = 0.06$ from *Kawai et al.* [1977] and $\alpha_T = 0.13$ from *Battjes et al.* [1987].

[8] Related recent work includes *Long and Resio* [2007], who examine equilibrium range bandwidth under different fetch-limited conditions and directional cases, and *Takagaki et al.* [2012], who show a relation between the wind stress and spectral levels of both the equilibrium range and the swell range.

[9] Here, we extend the results of *Juszko et al.* [1995] to a much larger data set and include detailed observations of the equilibrium balance in equation (1), where $0 = S_{wind} - S_{brk} + S_{nl}$. The primary data are process measurements with drifting buoys and shipboard instruments in the vicinity of OWS-P during a 3 week research cruise. The secondary data long-term mooring observations from Ocean Weather Station P (OWS-P), an ongoing reference site at 50°N 145°W in the North Pacific Ocean. The site has long been used to study air–sea interaction [e.g., *Large and Pond*, 1981], because of its deep location, weak currents, and large range of conditions.

[10] The data collection and processing are described in section 2. The results and sensitivities are in section 3. Errors and potential application are discussed in section 4. The conclusions are in section 5.

2. Methods

2.1. Shipboard and Drifter Observations

[11] Shipboard and drifting buoy data were collected during a mooring turnaround cruise in October 2012 aboard the R/V *New Horizon*, with a goal of directly observing equilibrium in the wave action balance (equation (1)). Three Surface Wave Instrument Floats with Tracking (SWIFTs) [see *Thomson*, 2012] were deployed to measure wave breaking dissipation in the vicinity of OWS-P (50°N 145°W). A three-axis sonic anemometer (RM Young model 8100) was temporarily mounted to the jackstaff at the bow of the R/V *New Horizon* to measure winds at 10 m height above the surface.

2.1.1. Turbulence Measurements and Calculation of Wave Breaking Dissipation S_{brk}

[12] The SWIFTs are drifters used to measure waves, winds, currents, and turbulence in a wave-following reference frame. The details of data collection and processing are described in *Thomson* [2012], and are only reviewed here.

[13] The primary SWIFT data used are pulse-coherent Doppler sonar (Nortek Aquadopp HR) profiles of turbulent velocities beneath the wave following surface, which is defined as $z_w = 0$. The turbulent velocities were collected at 4 Hz and were processed to estimate the second-order structure function of 5 min ensembles. The structure function is a direct spatial realization of the theoretical *Kolmogorov* [1941] energy cascade from large to small scales. Fitting the observed structure function to $\mathcal{A}r^{2/3}$, where r is the spatial separation of velocity measurements along a profile, is equivalent to fitting a $k^{-5/3}$ wave number spectrum, and thus the turbulent kinetic energy (TKE) dissipation rates were estimated according to *Wiles et al.* [2006].

$$\epsilon_w(z_w) = \left(\frac{\mathcal{A}(z_w)}{C_v^2} \right)^{3/2}, \quad (7)$$

where $\mathcal{A}(z_w)$ is the amplitude determined for each depth below the wave surface z_w and $C_v^2 = 2.1$ is the constant commonly used in atmospheric studies of velocity structure [Sauvageot, 1992].

[14] Following Agrawal *et al.* [1992] and Gemmrich [2010], the total TKE dissipation is predominantly from wave breaking (i.e., $\epsilon_{brk} \approx \epsilon_w$) and mostly constrained to within the first meter beneath a breaking crest ($z_w < -1$ m). Thus, the wave-breaking loss term in the wave-action balance (equation (1)) is approximated as

$$\int S_{brk} df \approx \rho_w \int \epsilon_{brk} dz_w, \quad (8)$$

where the radian frequency integral on the left-hand side is over the entire equilibrium range, because the SWIFT estimates of ϵ_{brk} are not localized in frequency.

2.1.2. Wind Stress Measurements and Calculation of Wind Input S_{wind}

[15] The sonic anemometer data from the jackstaff of the R/V *New Horizon* were collected at 10 Hz and despiked using the phase-space method of Goring and Nikora [2002] and Mori *et al.* [2007]. Approximately 0.5% of all points are rejected during despiking. The sonic data were processed in 10 min windows according to the direct eddy covariance method of Edson *et al.* [1998] and according to the dissipation method of Yelland *et al.* [1994].

[16] In the direct eddy covariance method, wind friction velocity was estimated by

$$u_* = \sqrt{\langle u'w' \rangle}, \quad (9)$$

where u' and w' are turbulent horizontal and vertical functions of velocity, after removal of ship motion using data from a collocated accelerometer.

[17] To assess the potential for residual motion contamination in the covariance calculation, a second method for wind friction velocity was also used, in which an air-side dissipation rate ϵ_a was estimated from turbulence spectra and then used to calculate the wind friction velocity u_* . The time series were parsed into 128-point windows that were tapered with a Hamming window and overlapped 50%, then fast Fourier transformed. Ensemble spectra were made at 10 min intervals by averaging 46 windows to obtain final spectra with 0.0391 Hz frequency resolution. The ensemble spectra were fit to an expected frequency dependence of $f^{-5/3}$ in the inertial subrange ($1 < f < 4$ Hz), and the air-side dissipation was estimated assuming advection of a frozen field (Taylor's hypothesis) at a speed U_{10} , such that

$$\epsilon_a = \left(\frac{\langle E(f) f^{5/3} \rangle}{K \left(\frac{U_{10}}{2\pi} \right)^{2/3}} \right)^{3/2} \quad (10)$$

where $K = 0.55$ is the horizontal Kolmogorov constant. Assuming neutral stability, the wind friction velocity is then

$$u_* = (\kappa \epsilon_a z)^{1/3}, \quad (11)$$

where $\kappa = 0.4$ is the von Karman constant and $z = 10$ is the measurement height above the still water level.

[18] Following Phillips [1985], the wind input term in the wave action balance scales with the wind stress and the speed of the waves. Integrating over the equilibrium frequency range, the total wind input is then [Gemmrich *et al.*, 1994; Terray *et al.*, 1996]

$$\int S_{wind} df = c_e \tau = c_e \rho_a u_*^2, \quad (12)$$

where $c_e = 3$ m/s is the chosen effective energy transfer speed (constant throughout), which is the middle of the equilibrium range under most conditions. This choice is at the upper end of the scaling from Hwang [2009] and obscures the dependencies therein.

2.2. Mooring Observations

[19] Wave spectral data were collected at OWS-P using a 0.9 m Datawell directional waverider (DWR MKIII) buoy owned by the Applied Physics Laboratory at the University of Washington (APL-UW). The buoy was moored in 4255 m water depth at 49.985°N 145.094°W from 15 June 2010 until recovery on 4 October 2012. A replacement waverider mooring was deployed on 4 October 2012 at 49.904°N 145.243°W. These are the first spectral wave observations at OWS-P. (Previous wave observations were made visually by crewmen on weather ships, see Rutledge [1973]).

[20] The waverider collects buoy pitch, roll, and heave displacements at 1.28 Hz over half-hour intervals, then spectral moments are computed onboard. The spectra are transmitted via Iridium satellite modem to the Coastal Data Information Program (CDIP) at the Scripps Institution of Oceanography, where the data are publicly available as Station 166. The data are also posted under the National Data Buoy Center (NDBC) as Station 46246. There are 33,665 spectra used (from the original 2 year deployment) in this study.

[21] The upper portion (surface to 150 m depth) of the mooring includes a 30 m rubber cord and 3:1 scope ratio, such that the waverider can move freely and follow the waves. The lower portion (150–4255 m depth) is tensioned by a subsurface float, such that the mooring has a small watch circle (<1000 m) despite the substantial depth of the location.

[22] Meteorological data were collected at OWS-P from a separate mooring, operated by the Ocean Climate Stations (OCS) group at Pacific Marine Environmental Laboratory of the National Oceanic and Atmospheric Administration (PMEL-NOAA). This moored surface buoy was located 25–30 km from the APL-UW waverider mooring. The wind data are hourly values of component averages and gusts from a Gill sonic anemometer at 4 m height above the sea surface. The meteorological data are available from the NOAA OCS website (<http://www.pmel.noaa.gov/OCS>). The meteorological data use the oceanographic convention that wind direction is the direction toward (as opposed to from) which the wind is blowing.

2.2.1. Wave Spectral Measurements and Calculation of Equilibrium Friction Velocity u_*

[23] Wave energy frequency spectra $E(f)$ were calculated onboard the waverider buoy every half hour using eight 200 s long windows with no overlap, resulting in spectra with 0.01 Hz frequency resolution and 16 degrees of freedom. Wave directional moments, expressed as Fourier coefficients $a_1(f), b_1(f), a_2(f), b_2(f)$ at each frequency, were calculated from the cross spectra of heave, pitch, and roll [Kuik *et al.*, 1988]. Similar calculations are made from the SWIFT drifter buoy, following Herbers *et al.* [2012].

[24] Wave energy spectra $E(f)$ were used to calculate equilibrium friction velocity according to equation (2) by finding the average $8\pi^3 \langle f^4 E(f) \rangle$ in the equilibrium frequency range. The brackets indicate averaging over the equilibrium range, which was determined as the 20 neighboring frequency bands with the best fit to f^{-4} . The typical range was $0.2 < f_{eq} < 0.4$ Hz, except during very high winds when the range extended to $0.15 < f_{eq} < 0.35$ Hz. A variable lower limit was set as twice the frequency of the peak in the wind sea for each spectrum. A variable upper limit was set by requiring the Datawell “check” factor (the ratio of vertical to horizontal variance in buoy motion) to be within 5% of unity (as required for circular orbits and thus proper buoy response). A fixed upper limit of 0.4 Hz was also included to avoid strong Doppler modulation of very short waves by swell [Banner, 1990, 1991]. This modulation was avoided entirely in the freely drifting SWIFT measurements (Lagrangian reference frame). The standard error of $8\pi^3 f^4 E(f)$ in the equilibrium range was retained and propagated as a measure of uncertainty in each equilibrium u_* value.

[25] The average wave direction D_{eq} and directional spread ΔD_{eq} in the equilibrium range were computed as

$$D_{eq} = \arctan\left(\frac{\langle b_1(f) \rangle}{\langle a_1(f) \rangle}\right), \quad \Delta D_{eq} = \sqrt{2\left(1 - \sqrt{\langle a_1(f)^2 \rangle + \langle b_1(f)^2 \rangle}\right)}, \quad (13)$$

following [Kuik *et al.*, 1988], where the $\langle \rangle$ indicate averages over the equilibrium frequencies previously defined. These values were used to determine the relative alignment of the wind direction D_u to the equilibrium wave direction D_{eq} and the relative directional spread

$$\theta_{eq} = |D_u - D_{eq}|, \quad \Delta\theta_{eq} = \Delta D_{eq}, \quad (14)$$

and to approximate the directional function (in radians)

$$I(p) = \pi - \theta_{eq} - \frac{\Delta\theta_{eq}}{2}. \quad (15)$$

[26] This is in contrast to the slope ratio used by Juszko *et al.* [1995], and was chosen because of substantial noise in the slope ratio calculations.

[27] Finally, a canonical value $\beta = 0.012$ from the original Phillips [1985] study was used to determine the equilibrium wind friction velocity in equation (2). This usage is consistent with the findings of Juszko *et al.* [1995] and avoids any tuning of results.

2.3. WAVEWATCH III Modeling

[28] WAVEWATCH III [Tolman *et al.*, 2002; Tolman, 2009], is a third generation wave model developed at NOAA/NCEP (National Centers for Environmental Prediction) from the example of the WAM model [Group, 1988; Komen *et al.*, 1994], with initial development as WAVEWATCH occurring at the Delft University of Technology [Tolman, 1991]. WAVEWATCH III solves the random phase spectral action density balance equation (similar to equation (1)) for wave number-directional spectra. Being a phase-averaged model, there is an implied assumption that properties of the forcing, as well as the wave field itself, differ on space and time scales that are much larger than the variation scales of a single wave. For this study, a global simulation was conducted for the 4 month period, from 1 September 2010 to 1 January 2011. The first week is treated as an invalid period of “spin-up,” which is the shortest reasonable initiation time for Pacific waves (longer would be more conservative and appropriate for some applications). Excluding this period, the effective duration available for validation is 115 days total. Thirty six (36) directional bins are used, and 31 frequency bins, from 0.0418 to 0.73 Hz. A 0.5° geographic resolution is used. Sub-grid blocking by islands is accounted for using the method of Tolman [2003], with the so-called “obstruction grid” provided by the Fleet Numerical Meteorology and Oceanography Center (FNMOC). The bathymetry used here is also identical to that of the real-time global WW3 operational model at FNMOC. The nonstationary forcing fields consist of 10 m wind vectors and ice concentrations, both taken from the NCEP Climate Forecast System Reanalysis (CFSR) [Saha *et al.*, 2010]. During the past 5 years, WAVEWATCH III has evolved such that it can now be regarded as a community model, though primary responsibility and authority for the code is still with NOAA/NCEP. The actual model version used here is a development code, currently designated as WAVEWATCH III Version 4. For wind input, wave breaking, and swell dissipation source functions, the physics package of Ardhuin *et al.* [2010] is used. Details of these physics are not repeated here, except to point out where our model deviates from that one. Ardhuin *et al.* [2010] describe the TEST 441 variant of the new physics. In the present study, we use the more recent TEST 451 variant, which utilizes a minor improvement to the swell dissipation source function to provide a smooth transition between laminar and turbulent air flow in the boundary layer (equations (8) and (9) of that paper, respectively). In the Ardhuin *et al.* [2010] physics package, gross differences in biases (or lack thereof) of wind forcing fields are accommodated via the β_{max} parameter setting in the wind input source function, as noted in the Appendix of that paper. For the present study, we use $\beta_{max} = 1.23$ (the default setting is $\beta_{max} = 1.52$, being more appropriate for simulations forced by operational winds with significant negative bias). This choice of β_{max} is consistent with recent work applying CFSR winds [Rascle and Ardhuin, 2013].

3. Results

3.1. Shipboard and Drifter Results: Direct Evidence for Equilibrium

[29] Data from the October 2012 cruise are consistent with an equilibrium between wind input and breaking

dissipation at the high frequency range (0.2–0.4 Hz) of the wave energy spectrum. Using the bin-averaged results (from at least 6 h of raw data at each wind speed) of the shipboard anemometer and the SWIFTs, the wind friction velocities and associated wave action terms are in agreement over most of the range of observation conditions (3–12 m/s wind speeds).

[30] Figure 1a shows the scalar wave energy spectra from the SWIFTs, in which the spectral shape of f^{-4} is consistent and sorted by measured wind speeds. The equilibrium range extends to lower frequencies during the highest winds, consistent with the *Phillips* [1985] discussion of equilibrium wave numbers and forcing scales. This is also consistent with the heuristic expectation that only the waves with phase speeds c slower than the wind speed U (i.e., “young,” with the wave age $\frac{c}{U} < 1$) can be forced by the wind, and at high winds the range for which this occurs is broader. For each wind speed, an equilibrium wind friction velocity u_* is calculated using equations (2)–(6).

[31] Figure 1b shows the wind turbulent kinetic energy spectra from the shipboard sonic anemometer, in which the $f^{-5/3}$ inertial subrange is well represented and sorted by measured wind speeds. For each wind speed, a wind friction velocity u_* is estimated using equation (11) and the dissipation rate method described in section 2.1.1. Direction eddy correlation estimates of u_* are also used, and are similar to the inertial estimates. These methods avoid appli-

cation of a drag law or bulk parameterizations in validating the wave equilibrium results.

[32] Figure 1c shows strong agreement between the sonic friction velocities from the two methods and the equilibrium friction velocity. However, wave equilibrium values are biased low, relative to the sonic values, at higher winds. For the cruise data, the bias appears at 11 and 12 m/s, which were the highest winds observed. This is similar to the mooring results that follow, but occurs at more moderate wind speeds.

[33] Figure 1 also shows dynamic evidence for wave equilibrium in source/sink terms during the October 2012 mooring cruise. Application of the *Phillips* [1985] equilibrium assumes a local balance, in which both wave growth and flux divergence are small. In a further simplification, integration in frequency f over the equilibrium range removes the nonlinear term (because that term only redistributes energy in frequency), such that the balance in equation (1) reduces to wind input and breaking dissipation:

$$0 = \int S_{wind} df - \int S_{brk} df. \quad (16)$$

[34] The wave breaking dissipation profiles from SWIFTs during the October 2012 cruise are shown in Figure 1d and are also well sorted by measured wind speed. These values are integrated in depth (equation (8)) and

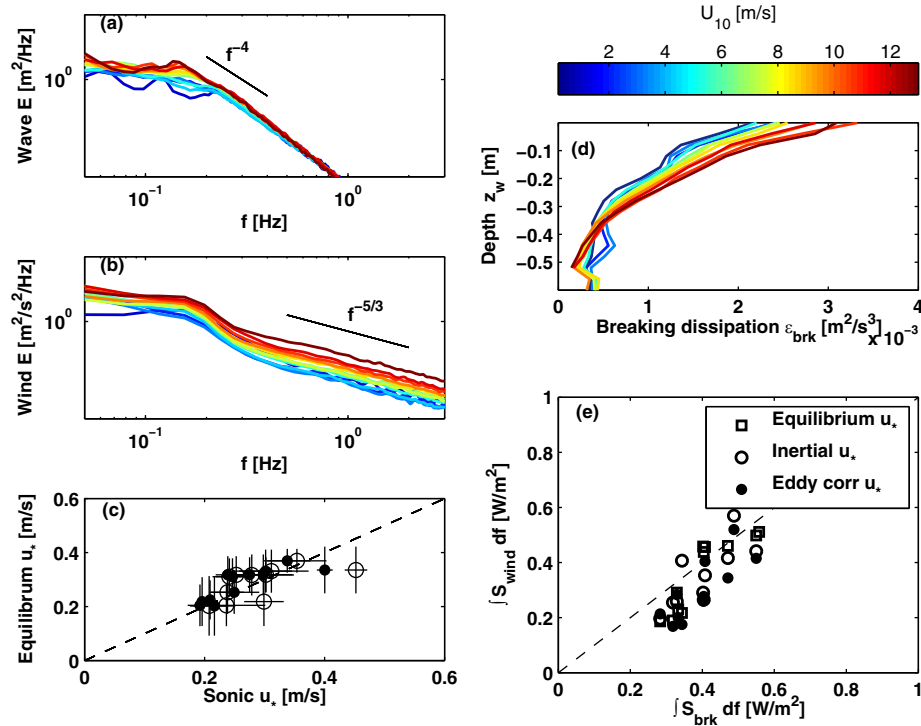


Figure 1. Results from the shipboard and drifter measurements during the October 2012 cruise, bin-averaged and colored by observed 10 m winds on the R/V *New Horizon*. (a) Wave energy spectra from SWIFT drifters. (b) Wind energy spectra from a shipboard sonic anemometer. (c) Comparison of wind friction velocity obtained via the wave equilibrium range and via the sonic anemometer using both the inertial dissipation method (open) and the direct eddy correlation method (closed). (d) Near-surface profiles of the wave breaking dissipation rate from SWIFT drifters. (e) Terms in the theoretical equilibrium balance of wind input and breaking dissipation. Thin lines indicate \pm one standard deviation from the binned averages.

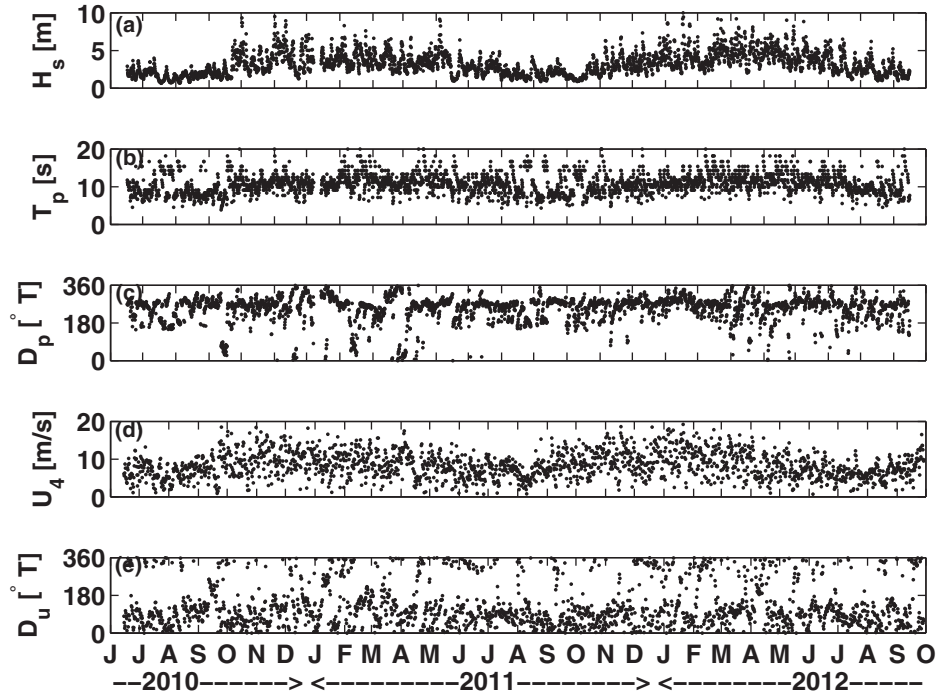


Figure 2. Hourly values for (a) significant wave height, (b) peak wave period, (c) peak wave direction, (d) wind speed, and (e) wind direction.

compared with the wind input (equation (12)) in Figure 1e, using both the wave equilibrium stress and the wind dissipation stress. Within measurement uncertainty, the expected equilibrium balance is observed for most conditions. Part of the scatter may be associated with variations in c_e , which is assumed fixed at 3 m/s in equation (12).

3.2. Mooring Results: Indirect Evidence for Equilibrium

[35] Figure 2 shows the 2 year time series of significant wave height, peak wave period, peak wave direction, wind speed, and wind direction. The time series includes a wide range of conditions, including pure wind seas, pure swell, and mixed seas. There is a strong seasonal signal, with the largest waves and longest periods occurring during the winter. This coincides with the strongest winds. The minimum observed significant wave height is 0.6 m and the maximum is 11.8 m.

[36] Figure 3 shows the hourly scalar wave energy spectra, colored by the wind speed observed at 4 m height, U_4 . The high frequencies with an observed f^{-4} dependence are the equilibrium range and are well sorted by the observed wind speeds. The lower frequencies are not sorted by winds, because these frequencies are dominated by the swells generated elsewhere that propagate through OWS-P. The equilibrium range wave energy spectra (i.e., the f^{-4} range) are used to calculate an equilibrium wind friction velocity u_* , following equations (2)–(6).

[37] Just as for the SWIFT drifter measurements, the f^{-4} dependence extends to lower frequencies during the highest winds (i.e., the scales of the equilibrium range, in addition to the amplitude, change with wind speed). Occasionally, the fit to f^{-4} is poor at all frequencies. This occurs for individual 30 min spectra during periods of rapidly changing

wind conditions, such that waves are strongly growing or decaying. Under these conditions, a dynamic equilibrium is not expected, and the observations have weak stationarity (i.e., the spectra may have higher uncertainty).

[38] Figure 4 shows the mean square slope (mss , equation (3)) of the wave spectral observations as a function of measured wind speed. There is a strong correlation, particularly for the mss at equilibrium frequencies. This is consistent with the Phillips [1985] prediction that wave spectral levels following $f^4 E(f)$ be directly tied to the local

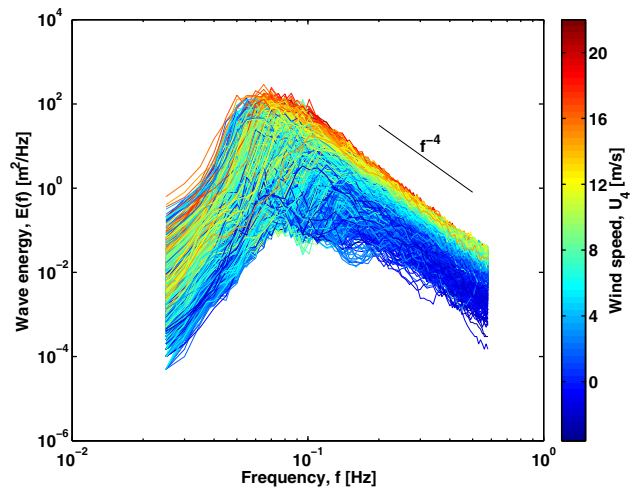


Figure 3. Hourly wave energy spectra from OWS-P buoy, colored by observed wind speed. The f^{-4} line indicates the theoretical spectral slope in the equilibrium range. Spectra in the equilibrium range are well sorted by observed wind speed.

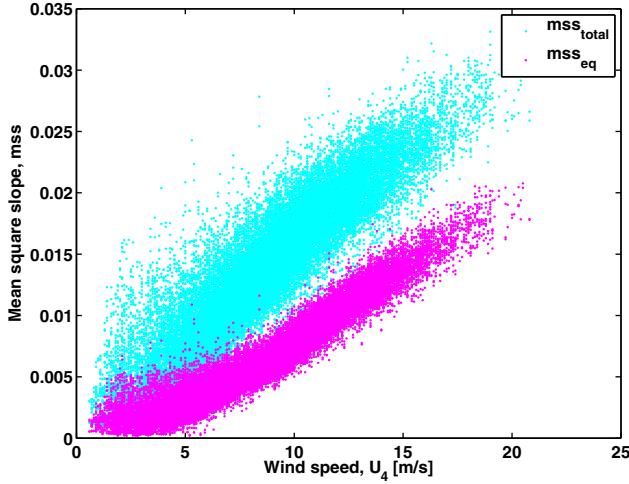


Figure 4. Mean square slope calculated from measured wave energy spectra versus measured wind speeds at 4 m height. Cyan points are calculated from all frequencies in each wave spectrum. Magenta points are calculated from equilibrium frequencies (twice the peak frequency and above) in each wave spectrum.

wind forcing, modulated by the the directional function $I(p)$ and the constant beta β .

[39] The relative direction of waves in the equilibrium range and the directional function $I(p)$ are shown in Figure 5. Waves in the equilibrium range are typically aligned with the wind ($\theta_{eq} \approx 0$), although there are notable deviations. The resulting $I(p)$ values are centered around 2.5, which Phillips [1985] noted as the expected result of directional index $p = \frac{1}{2}$.

[40] Figure 6 shows the equilibrium friction velocity u_* as a function of measured wind speed. Also shown are the equivalent wind friction velocities from conventional drag laws for wind stress, $u_* = C_D^{1/2} U_{10}$, where C_D is determined by measured wind speed [Smith, 1980; Large and

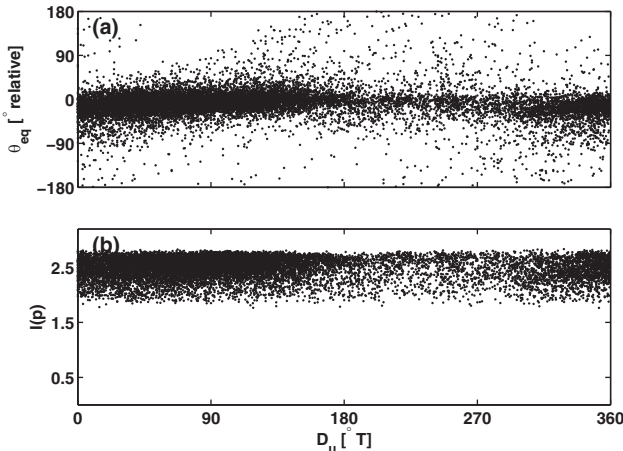


Figure 5. (a) Relative wave direction in the equilibrium range and (b) directional function versus observed wind direction. Equilibrium waves are expected to be aligned with the wind ($\theta_{eq} \approx 0$), and the canonical value of $I(p)$ is 2.5.

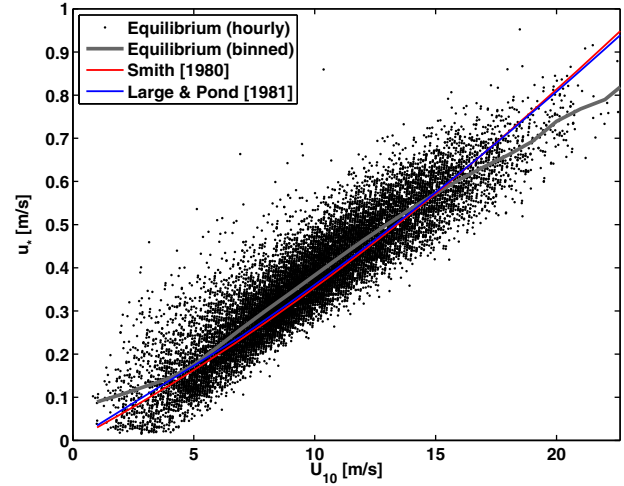


Figure 6. Equilibrium wind friction velocity (calculated from observed wave spectra) as a function of observed wind speeds, adjusted to 10 m reference height. Dots are hourly estimates from the equilibrium range of the observed wave spectra and the gray curve is the bin-averaged value at 1 m/s intervals. Red and blue lines are conventional drag law estimates.

Pond, 1981]. There is good agreement with conventional drag laws at most wind speeds ($r^2 = 0.91$, overall). Averaging in wind speed bins of 1 m/s, the equilibrium values are within 5% of the drag laws at most wind speeds. At the highest wind speeds, greater than 15 m/s, the equilibrium u_* values are less than the drag law estimates, and the bin-averaged values are biased low by up to 13%. At the lowest wind speeds, less than 5 m/s, the equilibrium u_* values are greater than the drag law estimates, and the bin-averaged values are biased high by up to 100%.

[41] The scatter of the equilibrium stress relative to the drag laws is evaluated in Figure 7, which shows spectra for three fixed wind speeds. At each wind speed, the spectra show a secondary dependence (the primary dependence being on wind speed itself) related to the equilibrium energy ratio, E_{eq}/E_{total} , which is unity for pure wind seas and approaches zero for swell dominated seas. Each spectrum is shown using frequencies normalized by the peak frequency, f_p , of that spectrum. The normalized wave spectra within a fixed wind speed are sorted such that spectra from pure wind seas have the lowest levels, and thus the lowest equilibrium wind stress. This oversimplifies the result, however, because the use of a normalized f/f_p shifts all pure wind seas to the left. The more general result is that the presence of swell modifies the response of the high frequency waves to wind forcing and is related to the scatter at a given wind speed.

[42] An equilibrium drag coefficient can be defined using the equilibrium u_* as in $C_D = \frac{u_*^2}{U_{10}^2}$ and is shown as a function of inverse wave age U_{10}/c_p and mean square slope mss in Figure 8, where drag is centered around the canonical 1.4×10^{-3} for young, steep waves. For older waves and lower slopes, there is large scatter in the drag coefficient, likely because waves in the swell range modulate the waves in the equilibrium range [García-Nava et al., 2012]. The scatter and the trends are well sorted by the equilibrium

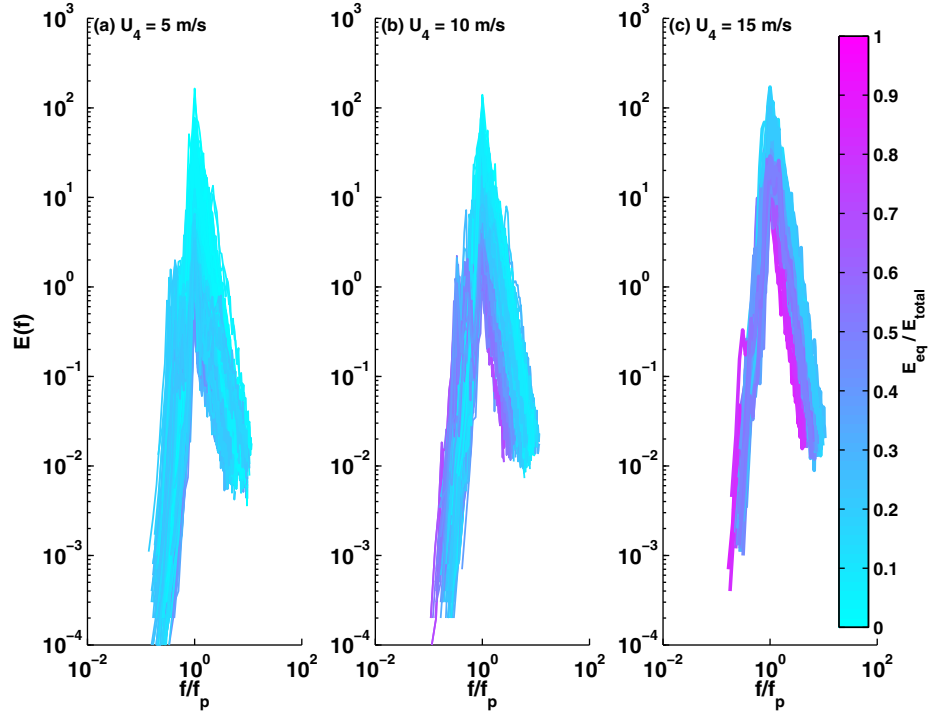


Figure 7. Wave energy spectra versus normalized frequency for three fixed wind speeds: (a) 5 m/s, (b) 10 m/s, and (c) 15 m/s. Frequencies in each spectrum are normalized by the peak frequency of that spectrum. Color scale indicates the ratio of wave energy in the equilibrium range to total wave energy. Magenta colors are pure wind seas and cyan colors are swell dominated.

energy ratio, E_{eq}/E_{total} . Figure 8 does not support the conventional trend of decreasing drag with increasing wave age [e.g., Donelan *et al.*, 1993], nor the pure slope dependence of Foreman and Emeis [2012]. Rather, Figure 8 shows

that the equilibrium drag dependence is more varied, especially for mixed seas and swell-dominated seas. The drag

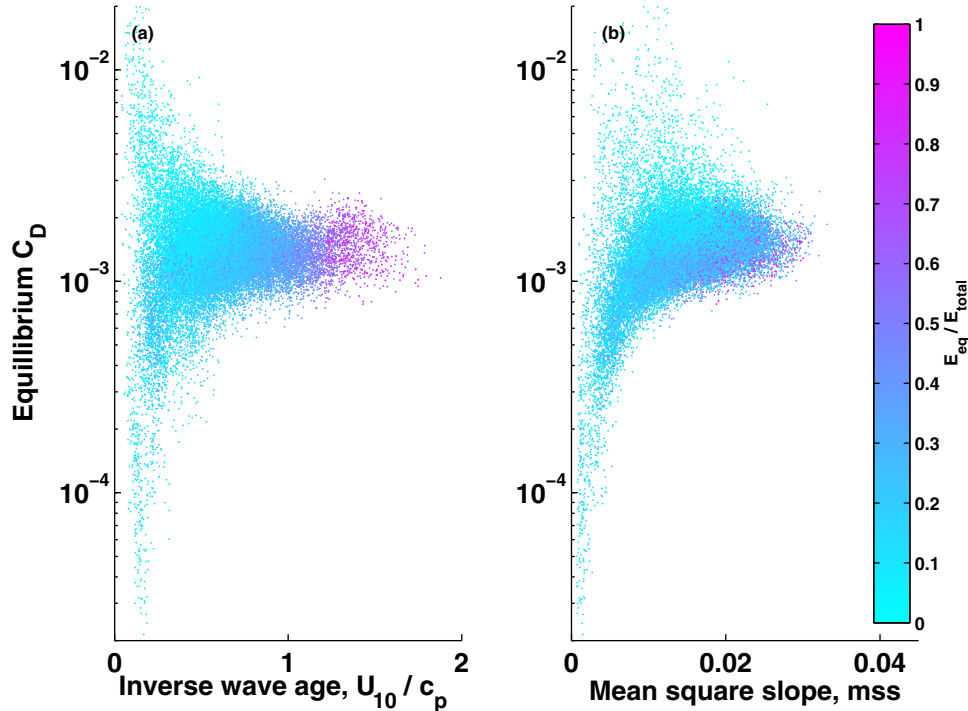


Figure 8. Equilibrium drag coefficient C_D as a function of (a) inverse wave age U_{10}/c_p and (b) mean square slope. Color scale indicates the ratio of wave energy in the equilibrium range to total wave energy. Magenta colors are pure wind seas and cyan colors are swell dominated.

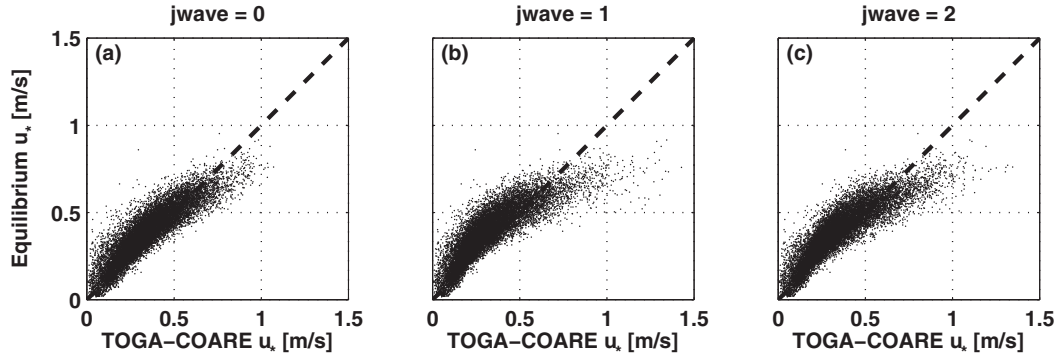


Figure 9. Hourly wind friction velocity from the equilibrium range compared with results from the COARE algorithm applied to observed meteorological data with (a) no wave dependence, (b) roughness dependent on wave age, and (c) roughness dependent on wave height and period. Dashed lines indicate 1:1 correspondence.

dependence on waves is further explored in *Toffoli et al.* [2012]. Here, of course, wave slope dependence is implicit given the equivalence of mean square slope and the equilibrium spectral level (i.e., equations (2) and (3)).

[43] To compare with the drag laws, the observed 4 m height winds are converted to 10 m height winds using the log-layer assumption (equation (4)) and a roughness length from the *Charnock* [1955] relation (equation (5)). This introduces a spurious correlation between U_{10} and the wave equilibrium estimate of u_* , because u_* is used to estimate roughness. However, the raw correlation of observed U_4 to u_* is already $r^2 = 0.90$ and the resulting correlation of adjusted U_{10} to u_* is $r^2 = 0.91$, so the additional correlation is negligible.

[44] It is tempting to examine the dependence of roughness z_0 on wave age $\frac{c_p}{u_*}$, as many previous investigations have done. However, in this case the spurious correlation is severe, as z_0 is uniquely determined by u_* in equation (5). Instead, the relation of roughness and u_* can be assessed indirectly with the estimates of wind stress from the COARE algorithm [Fairall et al., 2003].

[45] Figure 9 compares the equilibrium u_* to the results of the COARE algorithm (version 3.0a) [Fairall et al., 2003] using observed meteorological data and varying wave effects via the “*jwave*” parameter. For the standard algorithm with $jwave = 0$ (Figure 9a), the u_* estimates agree well at all but the highest values and have similar scatter to the drag law comparisons ($r^2 = 0.89$ for COARE versus $r^2 = 0.91$ for drag laws). When the wave-age dependent roughness of *Oost et al.* [2002] is included by setting the parameter $jwave = 1$ (Figure 9b), the model results at high winds are biased higher relative to the equilibrium u_* and scatter is slightly increased ($r^2 = 0.84$). When the wave height and period dependent roughness of *Taylor and Yelland* [2001] is included by setting the parameter $jwave = 2$ (Figure 9c), the model results at high winds also are biased higher relative to the equilibrium u_* , with similar scatter $r^2 = 0.88$. The scatter is not reduced by the inclusion of advanced wave-drag parameterizations in COARE, which suggests that the scatter may be independent of wave effects.

[46] The relative uncertainty of u_* is quantified by comparing the standard error of $\langle f^4 E(f) \rangle$ to its mean value, as

shown in Figure 10 as a function of measured wind speed U_4 and the directional function $I(p)$. The relative error is typically less than 2%, although sometimes as high as 5% for low winds. There is no correlation between the uncertainty and the directional function $I(p)$.

3.3. Model Comparison

[47] A spectral hindcast using the WAVEWATCH III model [Tolman and Chalikov, 1994] for the fall of 2010 shows excellent agreement with the waverider mooring observations (Figure 11). Comparing the bulk wave statistics, there is excellent agreement in wave heights ($r^2 = 0.96$) and significant agreement in peak wave direction ($r^2 = 0.68$, ignore wrapping within $\pm 30^\circ$ of North) and peak wave period ($r^2 = 0.67$). Bulk parameter prediction skill of the developmental hindcast (WW3 version 4) is notably better than that of the operational hindcast (which are $r^2 = 0.91$, 0.53, and 0.35, respectively). This suggests that the *Ardhuin et al.* [2010] formulations applied within the WW3 version 4 development code, as well as the use of

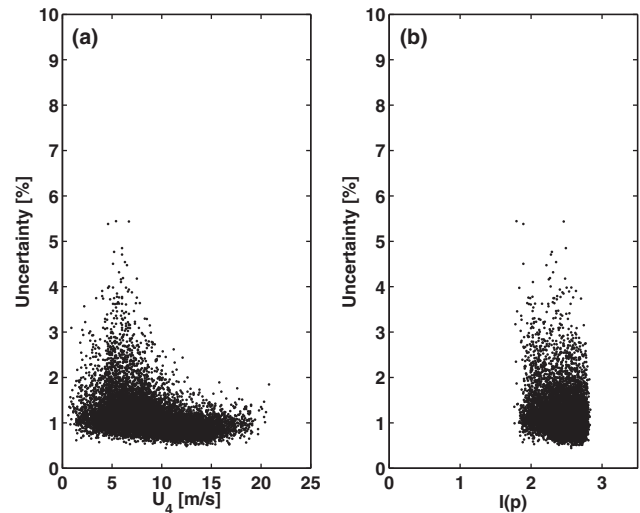


Figure 10. Relative uncertainty in equilibrium u_* as a function of (a) measured wind speed and (b) calculated directional function $I(p)$.

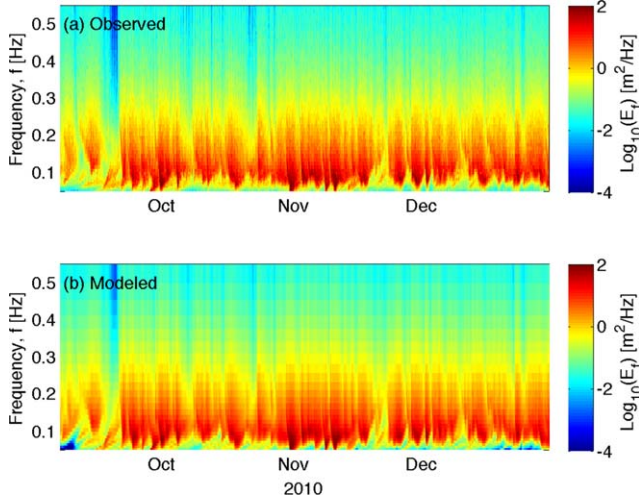


Figure 11. Spectragrams of wave energy (log color scale) in frequency versus time. (a) Datawell waverider mooring observations. (b) WAVEWATCH III model hindcast.

reanalysis winds, are to be preferred. The model deficiencies are associated with southward directions, which coincide with regionally generated wind seas from the Gulf of Alaska.

[48] Figure 12 shows the wave equilibrium u_* estimates from the model and the mooring data. There is excellent agreement ($r^2 = 0.88$), however there is a mild discrepancy for the most energetic conditions. At the highest winds, the model wind stresses are slightly higher than the equilibrium stress. Independent model runs with ECMWF winds show a similar monotonic increase in stress and waves at higher winds [Rascle and Ardhuin, 2013].

[49] Figure 13 shows the spectral input term from WW3 versus u_*^2 , which is the assumed input scaling in analysis of the field measurements (equation (12)). Input at high frequencies follows the assumed u_*^2 dependence under all but the milder conditions. Input over all frequencies is more scattered, consistent with the secondary dependences on the swell conditions.

4. Discussion

[50] The f^{-4} shape in wave spectra observed across all wind and wave conditions (Figure 3) and the small relative error of this shape (Figure 10) show the persistence of the equilibrium range. However, the very highest frequencies often have a steeper dependence, approximately f^{-5} , similar to the observations by Long and Resio [2007]. This may indicate something missing in the Phillips [1985] formulation, or it may be the damped response of finite size buoys at very high wave numbers (i.e., measurement error).

[51] Although the overall agreement between the equilibrium u_* and drag laws applied to the observed winds is compelling, there is notable scatter in Figures 6 and 9. The scatter may be attributed to atmospheric stability or wave age dependence in roughness, both of which alter the observed wind speed at a given height (4 m at OWS-P) for the same u_* . In either case, it would be the wind profile U_z that changes, not the surface stress $\tau = \rho_a u_*^2$. For a given

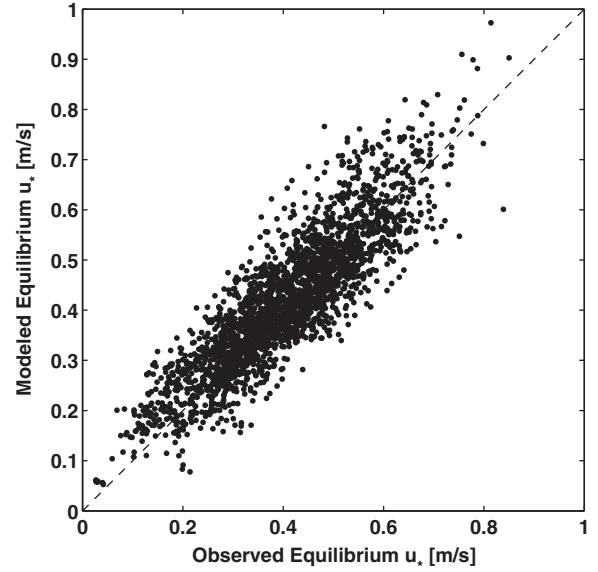


Figure 12. Equilibrium wind friction velocities from WAVEWATCH III model hindcast spectra versus equilibrium wind friction velocities from observed wave spectra. The correlation is $r^2 = 0.88$.

stress, equilibrium requires the high frequency waves to rapidly and continually adjust to maintain a balance with the winds. A lag-correlation analysis (not shown) indicates that the winds and waves are coherent and in phase for time scales from 1 h to several days, with no relation to the scatter around the drag laws.

[52] An alternative interpretation to the scatter in u_* is variation in the parameter β , which has been assumed constant at the canonical value $\beta = 0.012$. In both Juszko et al. [1995] and the present study, allowing a variable β does

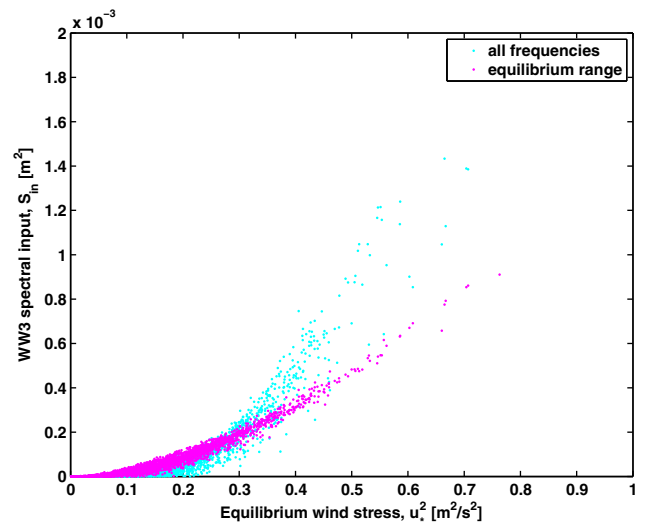


Figure 13. Spectral input terms from WAVEWATCH III versus equilibrium wind friction velocity squared. Cyan points are calculated from all frequencies in each wave spectrum. Magenta points are calculated from equilibrium frequencies (twice the peak frequency and above) in each wave spectrum.

not systematically improve the comparison to drag laws, thus the original value from Phillips [1985] is preferred.

[53] At the highest winds, there is an approximately 13% bias low in equilibrium u_* values relative to drag law estimates ($U_{10} > 15$ m/s in Figure 6) and the COARE results ($u_* > 0.8$ m/s in Figure 9). This occurs at wind speeds around 15 m/s, which is too low for the reported saturation and reduced drag at extreme winds [e.g., Powell et al., 2003; Jarosz et al., 2007; Black et al., 2007]. The most likely explanation is a known statistical bias of bin-averaging the highest (and rarest) values of a distribution [Tolman, 1998]. Another possible explanation is that storm conditions include elevated spectral energy levels at swell frequencies and those modulate the spectral energy levels at equilibrium frequencies (and thus bias the comparison to measured winds). From the mooring data, it is not possible to determine the atmospheric drag directly (a roughness estimate, or measurements of the U_z profile, are needed), so the results at high winds cannot be fully diagnosed. From the SWIFT data (Figure 1), the dynamic balance of wave equilibrium appears to continue at least up to 12 m/s.

[54] However, the range of the dynamic terms S_{wind} and S_{brk} is limited. These values are difficult to determine experimentally, in part because they vary by less than an order of magnitude from mild conditions to rough seas (although it should be noted that the October 2012 cruise data do not include any pure calm seas or extreme storms). More striking, it is the net difference between these variables that gives the evolution of a wave field, and that net difference is only significant over large amounts of space and time.

[55] Finally, a potential application deserves comment. The implication of equation (2) is that, given β , wind friction velocity u_* (and thus wind stress) could be determined from wave energy spectra alone. Such a future application requires validation of the Phillips [1985] theory (equation (2)), and it will require knowledge of the alignment and directional spread of waves relative to the wind, as given by $I(p)$ and shown in Figure 5. However, in practice, $I(p)$ does not vary much over the entire range of observations at OWS-P. If one assumes no knowledge of directionality, and instead uses a constant $I(p) = 2.5$ from the approximation $p = \frac{1}{2}$ (see Figure 2 of Phillips [1985]), the u_* results are similar. The average change in u_* is 6%, which is significant compared with the 2% uncertainty in $8\pi^3 \langle f^4 E(f) \rangle$, but no worse than the scatter relative to the drag laws.

5. Conclusions

[56] Observations of the wave equilibrium range provide evidence of a dynamic balance in which wave breaking adjusts to balance a given wind stress input, at least for wind speeds less than 12 m/s. Using 2 years of observations spanning a wide range of conditions, bin-averaged equilibrium results for wind stress are within 5% of the conventional drag laws based on U_{10} wind speeds [Smith, 1980; Large and Pond, 1981]. There is limited sensitivity (6%, on average) to the wind-wave alignment or directional spread of the waves. A secondary dependence is noted, wherein swell waves modify the high-frequency response to a given wind forcing.

[57] **Acknowledgments.** Joe Talbert (APL-UW) designed and built the waverider mooring, with guidance from Christian Meinig (PMEL-NOAA) and assistance from Alex deKlerk (APL-UW) and Stephanie Downey (APL-UW). Marie Roberts (IOS Canada) and the crew of the R/V *Tully* deployed the original mooring. Julie Thomas and Grant Cameron (CDIP-SIO) provided the waverider data telemetry and data archiving. Wind data were provided by the PMEL-NOAA Ocean Climate Stations group, with assistance from Keith Ronnholm. The crew of the R/V *New Horizon* (SIO) helped with the October 2012 mooring turnaround. Michael Schwendeman (APL-UW) and Johannes Gemmrich (U. Victoria) have contributed many discussions on equilibrium waves. Two anonymous reviewers improved the analysis and discussion of results. Funding was provided by the National Science Foundation (OCE-0850551 and OCE-0960778).

References

- Agrawal, Y., E. A. Terray, M. A. Donelan, P. A. Hwang, A. J. Williams III, W. M. Drennan, K. Kahma, and S. A. Krtagorodski (1992), Enhanced dissipation of kinetic energy beneath surface waves, *Nature*, **359**, 219–220.
- Ardhuin, F., et al. (2010), Semi-empirical dissipation source functions for ocean waves: Part i, definitions, calibration and validations, *J. Phys. Oceanogr.*, **40**, 1917–1941.
- Banner, M. L. (1990), Equilibrium spectra of wind waves, *J. Phys. Oceanogr.*, **20**, 966–984.
- Banner, M. L. (1991), On the directional behavior of the equilibrium wave number spectrum: Implications for the equilibrium frequency spectrum, in *Directional Ocean Wave Spectra*, edited by Robert Beal, pp. 39–45, Johns Hopkins Univ. Press, Baltimore, MD.
- Battjes, J., T. Zitman, and L. Houlthuijsen (1987), Reanalysis of the spectra observed in JONSWAP, *J. Phys. Oceanogr.*, **17**, 1288–1295.
- Black, P. G., E. A. D'Asaro, T. B. Sanford, W. M. Drennan, J. A. Zhang, J. R. French, P. P. Niiler, E. J. Terrill, and E. J. Walsh (2007), Air–sea exchange in hurricanes: Synthesis of observations from the coupled boundary layer air–sea transfer experiment, *Bull. Am. Meteorol. Soc.*, **88**(3), 357–374.
- Charnock, H. (1955), Wind stress on a water surface, *Q. J. R. Meteorol. Soc.*, **81**, 639–640.
- Cox, C., and W. Munk (1954), Statistics of the sea surface derived from sun glitter, *J. Mar. Res.*, **13**, 198–227.
- Dobson, F., W. Perrie, and B. Toulany (1989), On the deep-water fetch laws for wind-generated surface gravity waves, *Atmos. Ocean*, **27**, 210–236.
- Donelan, M., J. Hamilton, and W. H. Hui (1985), Directional spectra of wind-generated waves, *Philos. Trans. R. Soc. London A*, **315**(1534), 509–562.
- Donelan, M., F. W. Dobson, S. D. Smith, and R. J. Anderson (1993), On the dependence of sea surface roughness on wave development, *J. Phys. Oceanogr.*, **23**, 2143–2149.
- Edson, J. B., A. A. Hinton, K. E. Prada, J. E. Hare, and C. W. Fairall (1998), Direct covariance flux estimates from mobile platforms at sea*, *J. Atmos. Oceanic Technol.*, **15**(2), 547–562.
- Fairall, C., E. Bradley, J. Hare, A. Grachev, and J. Edson (2003), Bulk parameterization of air–sea fluxes: Updates and verification for the COARE algorithm, *J. Clim.*, **16**, 571–591.
- Foreman, R., and S. Emeis (2012), Correlation equation for the marine drag coefficient and wave steepness, *Ocean Dyn.*, **62**, 1323–1333.
- García-Nava, H., F. J. Ocampo-Torres, P. A. Hwang, and P. Osuna (2012), Reduction of wind stress due to swell at high wind conditions, *J. Geophys. Res.*, **117**, C00J11, doi:10.1029/2011JC007833.
- Gemmrich, J. (2010), Strong turbulence in the wave crest region, *J. Phys. Oceanogr.*, **40**, 583–595.
- Gemmrich, J., T. Mudge, and V. Polonichko (1994), On the energy input from wind to surface waves, *J. Phys. Oceanogr.*, **24**, 2413–2417.
- Goring, D. G., and V. I. Nikora (2002), Despiking acoustic Doppler velocimeter data, *J. Hydraul. Eng.*, **128**(1), 117–126.
- Group, W. (1988), The WAM model—a third generation ocean wave prediction model, *J. Phys. Oceanogr.*, **18**, 1775–1810.
- Herbers, T. H. C., P. Jessen, T. Janssen, D. B. Colbert, and J. MacMahan (2012), Observing ocean surface waves with GPS tracked buoys, *J. Atmos. Oceanic Technol.*, **29**, 944–959.
- Hwang, P. A. (2009), Estimating the effective energy transfer velocity at air–sea interface, *J. Geophys. Res.*, **114**, C11011, doi:10.1029/2009JC005497.

- Jarosz, E., D. A. Mitchell, D. W. Wang, and W. J. Teague (2007), Bottom-up determination of air-sea momentum exchange under a major tropical cyclone, *Science*, **315**(5819), 1707–1709.
- Juszko, B. A., R. F. Marsden, and S. R. Waddell (1995), Wind stress from wave slopes using Phillips equilibrium theory, *J. Phys. Oceanogr.*, **25**, 185–204.
- Kawai, S., K. Okuda, and Y. Toba (1977), Field data support of three-seconds power law and $g\omega^{-4}$ spectral form for growing wind waves, *J. Oceanogr. Soc. Jpn.*, **33**, 137–150.
- Kitaigorodski, S. A. (1983), On the theory of the equilibrium range in the spectrum of wind-generated gravity waves, *J. Phys. Oceanogr.*, **13**, 816–827.
- Kolmogorov, A. N. (1941), Dissipation of energy in the locally isotropic turbulence, *Dokl. Akad. Nauk SSSR*, **30**, 301–305.
- Komen, G., L. Cavaleri, M. Donelan, K. Hasselmann, S. Hasselmann, and P. Janssen (1994), *Dynamics and Modelling of Ocean Waves*, Cambridge Univ. Press, Cambridge.
- Kuik, A. J., G. P. V. Vledder, and L. H. Holthuijsen (1988), A method for the routine analysis of pitch-and-roll buoy wave data, *J. Phys. Oceanogr.*, **18**, 1020–1034.
- Large, W., and S. Pond (1981), Open ocean momentum flux measurements in moderate to strong winds, *J. Phys. Oceanogr.*, **11**, 324–336.
- Long, C. E., and D. T. Resio (2007), Wind wave spectral observations in currituck sound, north carolina, *J. Geophys. Res.*, **112**, C05001, doi:10.1029/2006JC003835.
- Mori, N., T. Suzuki, and S. Kakuno (2007), Noise of acoustic Doppler velocimeter data in bubbly flow, *J. Eng. Mech.*, **133**(1), 122–125.
- Oost, W., G. Komen, C. Jacobs, and C. Van Oort (2002), New evidence for a relation between wind stress and wave age from measurements during asgAMAGE, *Boundary Layer Meteorol.*, **103**, 409–438.
- Phillips, O. M. (1985), Spectral and statistical properties of the equilibrium range in wind-generated gravity waves, *J. Fluid Mech.*, **156**, 495–531.
- Plant, B. (1982), A relationship between wind stress and wave slope, *J. Geophys. Res.*, **87**, 1961–1967.
- Powell, M. D., P. J. Vickery, and T. A. Reinhold (2003), Reduced drag coefficient for high wind speeds in tropical cyclones, *Nature*, **422**(6929), 279–283.
- Rascle, N., and F. Ardhuin (2013), A global wave parameter database for geophysical applications. Part 2: Model validation with improved source term parameterization, *Ocean Modell.*, **70**, 174–188, doi: 10.1016/j.oceanmod.2012.12.001.
- Rutledge, C. K. (1973), Processed wind and wave measurements from ocean weather station papa (1951–1971), Tech. Rep. R-73-010, Gen. Dyn. (Electronics Division), San Diego, CA.
- Saha, S., et al. (2010), The NCEP climate forecast system reanalysis, *Bull. Am. Meteorol. Soc.*, **91**(8), 1015–1056.
- Sauvageot, H. (1992), *Radar Meteorology*, 384 pp., Artech House, Norwood, Mass.
- Smith, S. D. (1980), Wind stress and heat flux over the ocean in gale force winds, *J. Phys. Oceanogr.*, **10**, 709–726.
- Takagaki, N., S. Komori, N. Suzuki, K. Iwano, T. Kuramoto, S. Shimada, R. Kurose, and K. Takahashi (2012), Strong correlation between the drag coefficient and the shape of the wind sea spectrum over a broad range of wind speeds, *Geophys. Res. Lett.*, **39**, L23604, doi:10.1029/2012GL053988.
- Taylor, P. K., and M. J. Yelland (2001), The dependence of sea surface roughness on the height and steepness of the waves, *J. Phys. Oceanogr.*, **31**(2), 572–590.
- Terray, E., M. Donelan, Y. Agrawal, W. Drennan, K. Kahma, A. Williams, P. Hwang, and S. Kitaigorodskii (1996), Estimates of kinetic energy dissipation under breaking waves, *J. Phys. Oceanogr.*, **26**, 792–807.
- Thomson, J. (2012), Wave breaking dissipation observed with SWIFT drifters, *J. Atmos. Oceanic Technol.*, **29**(12), 1866–1882.
- Toba, Y. (1973), Local balance in the air-sea boundary processes. III. On the spectrum of wind waves, *J. Oceanogr. Soc. Jpn.*, **29**, 209–220.
- Toffoli, A., L. Loffredo, P. L. Roy, J.-M. Lefèvre, and A. V. Babanin (2012), On the variability of sea drag in finite water depth, *J. Geophys. Res.*, **117**, C00J25, doi:10.1029/2011JC007857.
- Tolman, H., and D. Chalikov (1994), Development of a third-generation ocean wave model at NOAA-NMC, in *Proceedings of the International Symposium: Waves—Physical and Numerical Modeling*, edited by M. Isaacson, and M. C. Quick, pp. 724–733, Univ. of Br. Columbia Press, Vancouver.
- Tolman, H. L. (1991), A third generation model for wind-waves on slowly varying, unsteady, and inhomogeneous depths and currents, *J. Phys. Oceanogr.*, **21**(6), 782–797.
- Tolman, H. L. (1998), Effects of observation errors in linear regression and bin-average analyses, *Q. J. R. Meteorol. Soc.*, **124**(547), 897–917.
- Tolman, H. L. (2003), Treatment of unresolved islands and ice in wind wave models, *Ocean Modell.*, **5**, 219–231.
- Tolman, H. L. (2009), User manual and system documentation of WAVEWATCH III version 3.14, Technical Note 276, National Oceanic and Atmospheric Administration/National Weather Service/National Centers for Environmental Prediction/Marine Modeling and Analysis Branch (NOAA/NWS/NCEP/MMAB), Camp Springs, MD.
- Tolman, H. L., B. Balasubramanian, L. Burroughs, D. Chalikov, Y. Chao, H. Chen, and V. Gerald (2002), Development and implementation of wind-generated ocean surface wave models at NCEP, *Weather Forecasting*, **17**, 311–333.
- Wiles, P., T. P. Rippeth, J. Simpson, and P. Hendricks (2006), A novel technique for measuring the rate of turbulent dissipation in the marine environment, *Geophys. Res. Lett.*, **33**, L21608, doi:10.1029/2006GL027050.
- Yelland, M., P. Taylor, I. Consterdine, and M. Smith (1994), The use of the inertial dissipation technique for shipboard wind stress determination, *J. Atmos. Oceanic Technol.*, **11**, 1093–1108.
- Young, I. (1999), *Wind Generated Ocean Waves*, Elsevier, New York.